



HAL
open science

Katabatic Winds over Steep Slopes: Overview of a Field Experiment Designed to Investigate Slope-Normal Velocity and Near-Surface Turbulence

Claudine Charrondière, Christophe Brun, Jean-Martial Cohard,
Jean-Emmanuel Sicart, Martin Obligado, Romain Biron, Catherine Coulaud,
Hélène Guyard

► To cite this version:

Claudine Charrondière, Christophe Brun, Jean-Martial Cohard, Jean-Emmanuel Sicart, Martin Obligado, et al.. Katabatic Winds over Steep Slopes: Overview of a Field Experiment Designed to Investigate Slope-Normal Velocity and Near-Surface Turbulence. *Boundary-Layer Meteorology*, 2022, 182 (1), pp.29-54. 10.1007/s10546-021-00644-y . hal-03350043

HAL Id: hal-03350043

<https://hal.science/hal-03350043v1>

Submitted on 6 Apr 2022


HAL is a multi-disciplinary open access archive for the deposit and dissemination of scientific research documents, whether they are published or not. The documents may come from teaching and research institutions in France or abroad, or from public or private research centers.

L'archive ouverte pluridisciplinaire **HAL**, est destinée au dépôt et à la diffusion de documents scientifiques de niveau recherche, publiés ou non, émanant des établissements d'enseignement et de recherche français ou étrangers, des laboratoires publics ou privés.



Distributed under a Creative Commons Attribution - NonCommercial 4.0 International License

Katabatic Winds over Steep Slopes: Overview of a Field Experiment Designed to Investigate Slope-Normal Velocity and Near-Surface Turbulence

Claudine Charrondière^{1,2}  · Christophe Brun¹ · Jean-Martial Cohard² · Jean-Emmanuel Sicart² · Martin Obligado¹ · Romain Biron² · Catherine Coulaud² · H  l  ne Guyard²

Abstract

We describe a new field campaign over a steep, snowy 30° alpine slope, designed to investigate three recurrent issues in experimental studies of steep-slope katabatic winds. (1) Entrainment is known to be present in katabatic jets and has been estimated at the interface between the jet and the boundary layer above it. However, to our knowledge, the slope-normal velocity component has never been measured in the katabatic jet. (2) It is hard to accurately measure turbulence in the first tens of centimetres above the surface using standard sonic anemometry due to the filtering effect of the long instrument path. The present field experiment used a three-dimensional multi-hole pitot-type probe with a high sampling frequency (1250 Hz) that was positioned as close to the surface as 3 cm. It provides three-dimensional mean velocity and Reynolds stress tensor from which dissipation can be estimated, as well as spectra for the turbulent quantities. Energy spectra reveal a well-developed inertial range and capture the inertial scales and some of the dissipative scales. (3) Measuring turbulence on a mast usually provides information about mean and turbulent quantities at certain discrete heights because the sensors are sparsely located inside the jet. We present the first measurements of well-developed katabatic flows where the full wind-speed and temperature profiles acquired, from tethered balloon are available at the location of the measurement mast, which comprises three-dimensional anemometry and thermometry.

Keywords Field experiment · Katabatic jet · Near-surface turbulence · Slope-normal velocity · Steep alpine slope

✉ Claudine Charrondière
charrondiere.claudine@gmail.com

¹ Laboratoire des   coulements G  ophysiques et Industriels (LEGI), Grenoble, France

² Institut des G  osciences de l'Environnement (IGE), Grenoble, France

1 Introduction

Katabatic winds were first discussed in the scientific literature in the 1840s (Poulos and Zhong 2008) followed by some observational reports in the 1920–1930s and by modelling and prediction of their main characteristics in the 1940s (Finnigan et al. 2020). Today interest in downslope flows is ever increasing because they play a role in many societal issues including air quality (e.g., Low 1990; Whiteman 2000; Largeron and Staquet 2016), surface energy budgets that have been the subject of studies of the impacts of climate change on glaciers (e.g., Duynkerke and Van den Broeke 1994; Van Den Broeke et al. 1994; Litt et al. 2017) and weather forecasts (Steenveld et al. 2010). Furthermore, the large temperature and velocity gradients close to the surface affect interfacial exchanges between the surface and the planetary boundary layer, which ultimately controls mountain ecosystems (Baldochi 2003; Sun et al. 2010). Thus, many scientific challenges are involved, including how to represent katabatic flow in numerical modelling as well as how small-scale processes and mesoscale or synoptic scales interact, among others.

Many experimental studies of katabatic flows have been conducted over gentle slopes (e.g., Smeets et al. 1998; Monti et al. 2002; Haiden and Whiteman 2005; Litt et al. 2015; Grachev et al. 2016; Jensen et al. 2017; Stiperski et al. 2020, as well as references in Poulos and Zhong 2008), but only a few in situ studies were conducted over slopes of more than 20° (Horst and Doran 1988; Nadeau et al. 2013a; Oldroyd et al. 2014, 2016a; Charrondière et al. 2020). On such steep slopes, the vertical axis related to buoyancy forcing differs significantly from the slope-normal axis. This characteristic cannot be ignored when studying the effect of buoyancy on turbulence kinetic energy (TKE, Oldroyd et al. 2016a; Charrondière et al. 2020). Moreover, the steeper the slope, the lower the maximum-wind-speed height (e.g., Prandtl 1942). This makes it difficult to characterize these jets using standard turbulence sensors such as sonic anemometers, especially in the inner layer close to the surface where the large separation of their paths prevents correct measurement of the relevant turbulence scales. Consequently, most of the aforementioned experimental katabatic studies over steep slopes mainly focused on the region above the maximum-wind-speed height, with limited extension in elevation. Only a few studies have tackled these widely shared scientific issues.

Rajaratnam (1976) citing Myers et al. (1961) states that the logarithmic velocity law is valid in the boundary-layer region of plane wall jets. Tachie et al. (2002) and Villafruela et al. (2008) also showed that the inner part of turbulent wall jets (below the maximum-wind-speed height) behaves in the same way as a turbulent boundary layer close to the surface. Katabatic jets are quite similar in structure to turbulent wall jets and they may develop logarithmic profiles in their lower part, possibly including marginal corrections due to buoyancy effects. However, this has never been observed for katabatic winds. In their study, Oldroyd et al. (2014) measured one level of wind speed at $z = 0.45$ m, below the maximum-wind-speed height, which was between the two measurement levels at 0.45 m and 1.27 m for a canopy height of about 30 cm. They showed that the presence of the canopy affects the length scale of thin katabatic jets (~ 1 -m deep) but concluded that measurements below the maximum-wind-speed height were unable to measure turbulence reliably. In Charrondière et al. (2020), one sonic anemometer was located at $z = 1$ m, below the maximum-wind-speed height at 1.36 m. These few references underline the scarcity of observations below the wind maximum, with no data on the first ten centimetres of the jet available in the literature. Observations are required in this region, particularly over steep slopes.

In addition to the lack of measurements in the lower part of the jet, turbulence and meteorological sensors on the masts are rarely positioned high enough to capture the return to zero

of the wind-speed profile predicted by the Prandtl model. Nadeau et al. (2013a) combined a tethered balloon with two turbulence masts to focus on the establishment of the katabatic flow during the evening transition. This needs to be studied more extensively, particularly in steady state conditions for comparison with theoretical models. Furthermore, the network of sensors of the i-Box (Innsbruck Box) project (Rotach et al. 2017) could provide insights into the spatial organization of such flows and their interactions over complex terrains, although this is not its primary goal.

The most appropriate coordinate system to use over a complex terrain is discussed by Sun (2007) and Oldroyd et al. (2016b). Since mean slope-normal wind shear acts parallel to the surface, it is conventional to consider a coordinate system that follows the topography. In practice, a coordinate system aligned with the streamlines is more often used in katabatic studies (e.g., Nadeau et al. 2013a; Grachev et al. 2016; Oldroyd et al. 2016a; Charrondière et al. 2020). This means that the coordinate system is not fixed in height or over time. This approach does not allow the slope-normal velocity component to be captured, since it is set to zero by construction. However, entrainment in katabatic flows has been accepted and reported for many years (e.g., Manins and Sawford 1979). Some studies (e.g., Van Den Broeke 1997; Princevac et al. 2005) estimated entrainment of air towards the katabatic jet at the interface between the jet and the layer directly above. Van Den Broeke (1997) indirectly estimated it over a glacier from closure of the integrated continuity moisture budget. He found entrainment velocity values between 0.7 and 2.4 cm s⁻¹. Princevac et al. (2005) show that the entrainment coefficient, defined as the ratio of entrainment velocity to a characteristic velocity scale, decreases with increasing stability. The slope-normal velocity component inside the jet has been directly measured in wall-jet studies (e.g., Eriksson et al. 1998, with laser Doppler anemometry in laboratory), and in the external region of gravity currents (Krug et al. 2013, using the particle image velocimetry technique in the laboratory). However, to our knowledge, such results are not available for katabatic jets.

This paper describes a dedicated field experiment designed to investigate the three aforementioned problematics: (1) studying inner-layer steep-slope katabatic jets requires time-resolved turbulence measurement in the first tens of centimetres above the surface; (2) studies of the connection between the katabatic jet and the planetary boundary layer require measurements between 10 and 100 m in height above the surface; (3) the usual streamline coordinate system results in nullifying the mean velocity in the slope-normal direction and does not enable investigation of this quantity inside the jet. To do so, measurements have to be made in a coordinate system associated with the topographic slope. The first results of the experiment are presented herein.

Section 2 describes the experimental design used to investigate slope-normal velocity profiles as well as near-surface wind velocity and turbulence. Section 3 describes the post-processing procedure applied to the data. Section 4 presents our first results with a focus on measurements of slope-normal velocity component, on the turbulent momentum flux profile, and on the inner-layer region of the jet. Finally, Sect. 5 summarizes all these preliminary results and reviews avenues for further investigation.

2 Presentation of the Field Experiment

2.1 Experimental Set-Up

A 10-m mast was set up on the west face of Grand Colon in the Belledonne mountain range (French Alps) from 12 to 28 February 2019, at an altitude of 1788 m above sea level (a.s.l., Site A on Fig. 1a). The local slope was estimated using a digital elevation model (DEM, BD ALTI IGN) of the region with 25-m horizontal resolution, $\alpha \simeq 30^\circ$. Eleven sonic anemometers and 10 thermocouples (Table 1) were attached to the mast as shown in Fig 1b, c. The bottom 35 cm of the mast were equipped with six thermocouples to ensure the precise measurement of the expected notable temperature gradient close to the surface. The six lowest three-dimensional sonic anemometers were attached to a mounting facility (Elcom, France). Mounting brackets ensured a fixed single tilt angle ($30^\circ \pm 1^\circ$) of the six sonic anemometers to the main Elcom structure (Fig. 1d). The lowest sonic anemometer (CSAT3B) was equipped with an inclinometer. The set-up was tailored to measure slope-normal velocity profiles.

To complement turbulent measurements below the maximum wind speed, we used a three-dimensional multi-hole pitot probe (Cobra probe, Turbulent Flow Instrumentation Pty Ltd, Australia). The size of the head (2.6 mm, Fig. 1e) made measurements possible down to $z = 3$ cm in height, with a measurement accuracy of 0.2 m s^{-1} in the range of wind speeds measured. High-frequency ($f = 1250 \text{ Hz}$) 1-min time series of three-dimensional velocity components were acquired between 0555 and 0636 local time (LT = UTC + 1 h) on 28 February 2019. The cobra probe was placed on a vertical bar inserted into the snow and was moved a few centimetres along this axis by hand between each series of measurements. This protocol guaranteed that the angle of inclination of the sensor was the same for all the measurements, within $\pm 1^\circ$.

To complement the wind-speed and temperature katabatic profiles above the mast and to estimate the thickness of the jet, we performed soundings using a tethered balloon system at the mast location (Site A) during eight nights of the experiment (15–17 February 2019 and 22–28 February 2019). One to eleven profiles per night, up to 50–100 m in height were performed. Measurements made by the balloon sensors concern pressure, temperature (in a ventilated compartment), relative humidity, and two-dimensional wind velocity (Table 1). The sensors mounted on the tethered balloon were set at an acquisition frequency ranging between 0.5 and 1 Hz, and its vertical displacement speed was of the order of 0.1 m s^{-1} . The height of on-board sensors was determined by air pressure P and temperature T measurements through the hydrostatic relationship $\Delta P = \rho g \Delta z$, integrated from the surface, where ρ is density from the perfect gas law, $P = \rho RT$ and $R = 287 \text{ J K}^{-1} \text{ kg}^{-1}$ for dry air.

When not used at Site A, the sensor block was attached to another tethered balloon at Site B in a clearing at a lower altitude than Site A (Fig. 1a, 1175 m a.s.l.). At Site B, the tethered balloon operated up to 300 m to provide information concerning synoptic thermal stability (see Sect. 3.1) and its vertical speed was around 0.3 m s^{-1} . The descent, realized with the help of a motorised hoist, was usually smooth and steadier than the manual ascent. The bottom few tens of metres of each profile were acquired more slowly than the upper part of the profile to account for the greater temperature gradient close to the ground, to better account for sensor response time (3–4 s).

Mean meteorological quantities (pressure, radiation fluxes, temperature, and relative humidity) were provided by a mast located 2 m away from the main turbulence mast, with a timestep of 10 min (Table 1). Surface temperature was estimated from the longwave radiation (LW) measurements, with the Stefan–Boltzmann law (Eq. 1, Davies et al. 1971),

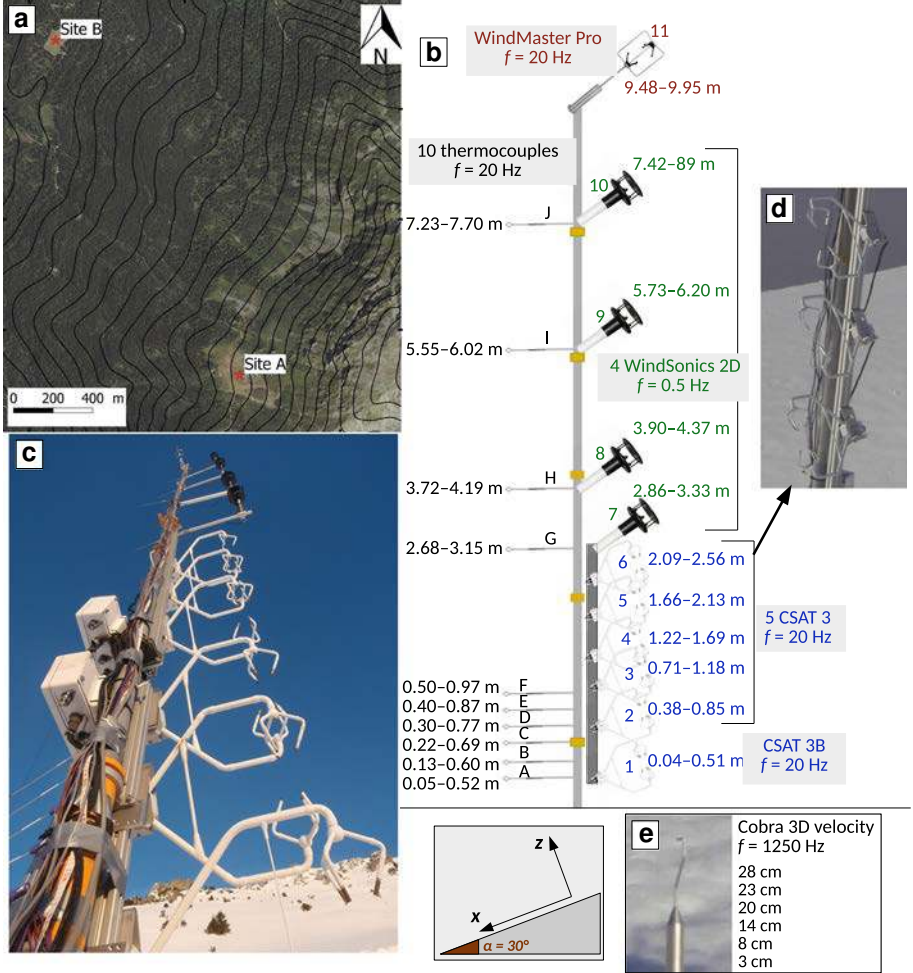


Fig. 1 **a** Location of Site A and Site B on a topographic map. **b** and **c** Structure of the turbulence mast. f is sampling frequency. The range of initial and final slope-normal height of each sensor along the field experiment is also presented. **d** CSAT fixing system. **e** Cobra pitot-type probe with its associated slope-normal measurement heights

where $\epsilon = 0.99$ is snow emissivity (e.g., Dozier and Warren 1982; Geiger et al. 2009) and $\sigma = 5.67 \times 10^{-8} \text{ W m}^{-2} \text{ K}^{-4}$ is the Stefan–Boltzman constant

$$T_s = \left(\frac{LW_{\text{up}} - (1 - \epsilon)LW_{\text{down}}}{\epsilon\sigma} \right)^{1/4}. \quad (1)$$

The surface was covered with 2 m of snow, and the last snowfall occurred the day before the beginning of the experiment. The snow melted and was packed, thereby reducing quasi-linearly the snow depth by about 50 cm over the course of the two-week measurement campaign. This caused variations in the measurement heights as the mast was set up on a rocky surface prior to the snowfall event. A sonic-ranging sensor (SR50, Table 1) measured changes in snow depth throughout the duration of the experiment.

Table 1 List of sensors attached to the masts and suspended from the tethered balloon

Sensor	Measured variables (accuracy)
<i>Turbulence mast</i>	
CSAT3B (Campbell Scientific, USA)	u, v (offset: $\pm 8 \text{ cm s}^{-1}$, gain: $\pm 2\%$), w (offset: $\pm 4 \text{ cm s}^{-1}$, gain: $\pm 2\%$), Sonic temperature Tilt angle ($\pm 1^\circ$)
CSAT3 (Campbell Scientific, USA)	u, v (offset: $\pm 8 \text{ cm s}^{-1}$, gain: $\pm 3\%$), w (offset: $\pm 4 \text{ cm s}^{-1}$, gain: $\pm 3\%$), Sonic temperature
WindMaster Pro (Gill instrument, England)	u, v, w ($\pm 1.5\%$), Sonic temperature ($\pm 2\%$)
Thermocouples FW3 type E (Campbell Scientific, USA)	Temperature ($\pm 1.7^\circ \text{C}$)
<i>Meteorological mast</i>	
CS100 (Campbell Scientific, USA)	Atmospheric pressure ($\pm 1 \text{ hPa}$)
CNR1 (Campbell Scientific, USA)	Longwave and shortwave radiation fluxes, downward and upward ($\pm 10\%$)
CS215 (Campbell Scientific, USA)	Temperature ($\pm 0.4^\circ \text{C}$) Relative humidity ($\pm 2\%$)
SR50 (Campbell Scientific, USA)	Height above the snow surface ($\pm 1 \text{ cm}$)
<i>Tethered balloon</i>	
BMP180 (Bosch, Germany)	Atmospheric pressure ($\pm 0.05 \text{ hPa}$)
HYT271 (Innovative sensor technology IST AG, Switzerland)	Temperature ($\pm 0.2^\circ \text{C}$) Relative humidity ($\pm 1.8\%$)
MCP9808 (Adafruit Industries, USA)	Temperature ($\pm 0.25^\circ \text{C}$)
WindSonic (Gill Instrument, England)	2D wind speed ($\pm 2\%$)

Accuracy is provided in the range of values observed during the experiment, according to the manufacturer. Wind-speed measurements of CSAT3 sonic anemometers were calibrated in a wind tunnel with respect to the CSAT3B sonic anemometer, so that the real accuracy is probably lower than that specified by the manufacturer.

The anticyclonic conditions that prevailed over the region during the field experiment favoured notable surface cooling at night as well as light synoptic winds. Reanalysis data, obtained from the Meteorological Institute in Berlin, Germany, show the three anticyclones successively established over the region (represented by different background colours in Fig. 4):

- Phase 1: from 12 February to 19 February 1200 LT. This high-pressure area was clearly stable in place and in pressure, with a pressure of around 1040 hPa in its centre.
- Phase 2: from 19 February 1200 LT to the night of 23–24 February. The highest sea-level pressure was 1030 hPa.
- Phase 3: from the night of 23–24 February to the end of the experiment. The highest sea-level pressure was 1040 hPa.

To place our field experiment in the context of steep slope measurements, Table 2 summarizes published experimental studies on the topic. The slope used for the present study is

Table 2 Characteristics of measurements acquired over steep slopes: slope angle α , surface sensible heat flux H_s and external stratification N_{ref} , maximum wind speed \bar{u}_j and height of the maximum z_j

	Forcing conditions and surface type	Characteristics of the jet
Blein (2016), Charrondière et al. (2020)	$\alpha = 21^\circ$ $-H_s = 50 \text{ W m}^{-2}$ $N_{ref} = 0.02 \text{ s}^{-1}$ Sparse small bushes and rocks	$z_j = 0.5 - 2 \text{ m}$ $\bar{u}_j = 2 - 3 \text{ m s}^{-1}$
Horst and Doran (1988)	$\alpha = 21^\circ$ Sparse sagebrush and desert grasses	$z_j = 1 \text{ m}$ $\bar{u}_j = 1 - 2 \text{ m s}^{-1}$
Nadeau et al. (2013a) Oldroyd et al. (2016a)	$\alpha = 30 - 41^\circ$ $-H_s = 20 - 30 \text{ W m}^{-2}$ $N_{ref} = 0.02 \text{ s}^{-1}$ 30 cm grass	$z_j < 1.5 \text{ m}$ $\bar{u}_j = 1 - 2 \text{ m s}^{-1}$
Present study	$\alpha = 30^\circ$ $-H_s = 15 - 45 \text{ W m}^{-2}$ $N_{ref} = 0.02 \text{ s}^{-1}$ Snow	$z_j = 0.2 - 1.2 \text{ m}$ $\bar{u}_j = 2 - 4 \text{ m s}^{-1}$
	Turbulence variables	Meteorological variables
Blein (2016), Charrondière et al. (2020)	u, v, w and T_{sonic} ($z = 1, 1.77, 3.98$ and 6.31 m)	T_s T and $RH(z = 1.59 \text{ m})$ $u, v(z = 3.08 \text{ m})$
Horst and Doran (1988)	u, v, w, T_{sonic} and T ($z = 1.77$ and 2.99 m)	T and $\ u\ $ ($z = 0.93, 2.15, 3.55, 5.04, 7.94, 12.14$ and 16.80 m) T and RH ($z = 1.8$ and 4.2 m [mast 1] and $z = 1.8 \text{ m}$ [mast 2])
Nadeau et al. (2013a), Oldroyd et al. (2016a)	u, v, w and T_{sonic} ($z = 1.5, 3.6, 4.7, 5.9 \text{ m}$ [mast 1] and $z = 2$ and 2.5 m [mast 2])	$\ \bar{u}\ $ ($z = 2.7 \text{ m}$) WD ($z = 2.3 \text{ m}$) $SW_{up}, SW_{down}, LW_{up}$ and LW_{down} ($z = 1.8$ and 2.1 m)
Present study	T ($z = 0.05, 0.13, 0.22, 0.30, 0.40,$ $0.50, 2.68, 3.72, 5.55$ and 7.23 m) u, v, w and T_{sonic} ($z = 0.04, 0.38, 0.71, 1.22, 1.66,$ 2.09 and 9.48 m)	$u, v(z = 2.86, 3.90, 5.73$ and $7.42 \text{ m})$ Meteorological mast (Table 1)

Symbols for variables are u, v , and w for the 3 components of wind velocity

SW and LW represent shortwave and longwave fluxes at the surface

Slope-normal height z for the present study is provided at the beginning of the field experiment

WD wind direction, T air temperature, T_s surface temperature, T_{sonic} sonic temperature, RH relative humidity

steeper than the slopes in Horst and Doran (1988) and Charrondière et al. (2020), and the slope angle α is of the same order of magnitude as that in Nadeau et al. (2013a) and Oldroyd et al. (2016a). To the best of our knowledge, this is the first study to be conducted over both a steep slope and a snow-covered surface.

2.2 Identification of Katabatic Events

All the data collected at night during the experiments were investigated to identify katabatic events based on the following criteria, as in Charrondière et al. (2020) and Stiperski et al. (2020):

1. The wind direction must be in the $-30^\circ, 30^\circ$ interval with respect to the main downslope direction.
2. Slope-normal profiles have to be consistent with the presence of a wall jet, with either a maximum wind speed or a decreasing trend of streamwise velocity if the maximum wind speed is not captured.
3. There must be a positive temperature gradient, and temperature should decrease strongly in the first metre above the ground.

These criteria identified a set of 13 katabatic events, the shortest lasting 30 min and the longest 3 h 15 min (Table 3). The first criterion ensures there is not too much external disturbance, and is the main reason for rejecting the data.

3 Post-processing of the Data

3.1 Ambient Stratification

Ambient thermal stratification was determined from the tethered balloon dataset acquired in the clearing (Site B, see Sect. 2.1). We discarded all profiles containing non-continuity or anomalies, which may signal gusts or stationarity issues. Temperature data from the thermohygrometer were converted into virtual potential temperature θ_v to account for pressure and humidity variability with height. The data were then used to determine thermal stratification of the atmosphere through the Brünt–Väisälä frequency N_{ref} following Eq. 2 (Stull 1988)

$$N_{ref} = \sqrt{\frac{g}{\theta_0} \partial_z \overline{\theta_v}}, \quad (2)$$

where $\partial_z \overline{\theta_v}$ is calculated along the vertical axis at site B and θ_0 is the potential temperature at ground level. A strong temperature gradient was observed near the surface, below $z = 30$ m (Fig. 2). The ambient stratification above was estimated with the upper temperature gradient.

3.2 Sonic Anemometers

In the following, $\overline{(\cdot)}$ represents temporal averaging over the length of each katabatic event, which lasted between 30 min and 3 h 15 min. $(\cdot)'$ is used for fluctuations around the average value following Reynolds decomposition: $(\cdot) = \overline{(\cdot)} + (\cdot)'$. Turbulent and mean characteristics were processed considering two sets of coordinate systems:

1. A streamline-defined coordinate system $(\vec{x}_s, \vec{y}_s, \vec{z}_s)$ based on the streamline orientation in such a way that $\vec{u} = \|\vec{u}\|$ and $\vec{v} = \vec{w} = 0$ at each sensor elevation (Wilczak et al. 2001). This coordinate system is often used in the literature because streamlines close to the surface are supposed to be nearly parallel to the topography and because in situ experiments rarely allow the exact inclination of each sensor to be determined (Horst and Doran 1988; Sun 2007; Nadeau et al. 2013b; Oldroyd et al. 2016b; Charrondière et al. 2020).

Table 3 Characteristics of katabatic events: air temperature θ and specific humidity q at $z \simeq 3.4$ m at the beginning of the experiment, surface temperature T_s , net radiation flux R_n

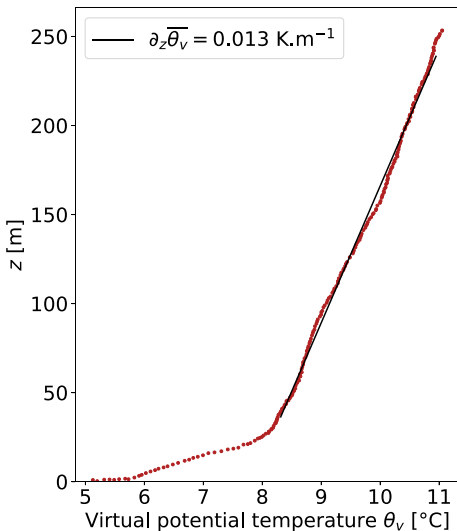
Name Time (LT)	$\bar{\theta}$ (°C) q (g kg ⁻¹)	T_s (°C) R_n (W m ⁻²)	z_j (m) \bar{u}_j (m s ⁻¹)	TKE(m ² s ⁻²)
1 13 February 1900–2140	3.4 ± 0.8 1.4 ± 0.07	- 7.5 ± 0.5 - 59 ± 3.5	0.23 3.3	0.11–0.14
2a 15 February 0430–0600	7.4 ± 0.18 1.5 ± 0.06	- 4.4 ± 0.12 - 63 ± 4	0.4 4.1	0.17–0.23
2b 15 February 0815–0915	7.5 ± 0.23 1.5 ± 0.06	- 4.8 ± 0.51 - 61 ± 1.4	0.39 4.1	0.16–0.21
3a 15 February 1710–1800	8.6 ± 0.39 2.7 ± 0.19	0.36 ± 0.47 32 ± 34.3	0.38 3.1	0.074–0.12
3b 15 February 1845–2015	7.4 ± 0.07 1.9 ± 0.17	- 2.4 ± 0.71 - 81 ± 4.6	0.41 3.5	0.14–0.21
3c 16 February 0130–0445	7.4 ± 0.17 1.5 ± 0.04	- 4.5 ± 0.28 - 72 ± 3	0.45 3.8	0.19–0.26
4 17 February 0400–0545	4.4 ± 0.27 1.6 ± 0.05	- 6.6 ± 0.37 - 74 ± 2	0.34 3.2	0.12–0.16
5 20 February 0500–0730	2.3 ± 0.08 2.2 ± 0.03	- 6.3 ± 0.35 - 61 ± 4	0.33 2.45	0.22–0.39
6a 23 February 1830–1900	5.9 ± 0.05 3 ± 0.09	- 1.6 ± 0.36 - 68 ± 3.8	1.1 3.3	0.11–0.14
6b 23 February 1920–2020	5.6 ± 0.12 3.1 ± 0.08	- 1.9 ± 0.31 - 67 ± 5.3	0.38 2.5	0.12–0.16
6c 23 February 2230–0045	3.9 ± 0.29 2.8 ± 0.11	- 4 ± 0.43 - 65 ± 2.1	0.3 2.3	0.09–0.13
6d 24 February 0500–0800	2.7 ± 0.42 2.8 ± 0.05	- 5.6 ± 0.51 - 64 ± 2.9	0.33 2.2	0.08–0.11
7 28 February 0530–0636	7.3 ± 0.23 2.1 ± 0.21	- 2.9 ± 0.41 - 64 ± 4.6	0.34–0.44 2.9	0.14–0.20 (0.07–0.17)

The data are the mean and the standard deviation of the 2-min segments of each event (See Sect. 3.2)

The maximum wind speed \bar{u}_j and its corresponding height z_j are given following the modified Prandtl model (Sect. 4.2, Brun et al. 2017; Charrondière et al. 2020)

The turbulence kinetic energy is the range measured in the external layer above z_j . The inner layer TKE is provided by the Cobra data for event 7 (in brackets)

Fig. 2 Virtual potential temperature profile from the tethered balloon at the clearing (Site B) on 15 February 2019 between 0905 and 0920 LT



2. A fixed coordinate system $(\vec{x}, \vec{y}, \vec{z})$, rotated by the topographic mean local angle derived from the DEM, $\alpha = 30^\circ$ with respect to the vertical in such a way that \bar{u} and \bar{w} are respectively the along-slope and the slope-normal velocity components in the coordinate system aligned with the mean local slope, like in Oldroyd et al. (2016a). The spanwise mean velocity \bar{v} was nullified by rotation. This coordinate system makes it possible to measure variations of quantities with height on a common axis and is the most objective choice, considering flow dynamics over complex terrain. This coordinate system was used only for the six lowest sonic anemometers, because they are the only ones for which we know the systematic orientation (Sect. 2.1).

Sonic anemometers were oriented parallel to the main topography to limit flow distortion. In the optimal configuration, the angle between streamlines and CSAT paths is 60° , which we approach by less than 10° during katabatic events, due to the presence of non-zero \bar{w} (Sect. 4.3). In this case, the flow distortion causes an error that is less than 5% of mean velocity (Horst et al. 2015).

Reynolds decomposition was applied to the high-frequency data recorded by the three-dimensional sonic anemometers, with a 2-min averaging time determined by multi-resolution flux decomposition (MRD, Fig. 3a, Howell and Mahrt 1997; Vickers and Mahrt 2003). This 2-min period was found to be the best compromise to separate the turbulent scales from the mesoscale motions at this site during periods with stable conditions (Blein 2016; Charrondière et al. 2020). Mean flow oscillations with a period of about $N_{ref} \sin \alpha$ (McNider 1982) have been extensively observed in katabatic flows (e.g., Helmis and Papadopoulos 1996; Princevac et al. 2008) and are consistently reproduced by numerical modelling (e.g., Fedorovich and Shapiro 2009; Shapiro and Fedorovich 2014). In the observed events, they had over a period between 10 and 20 min (Fig. 3). While their presence can still be observed in the mean field due to the rotation applied on the whole time series, turbulent fluxes are not affected by these oscillations.

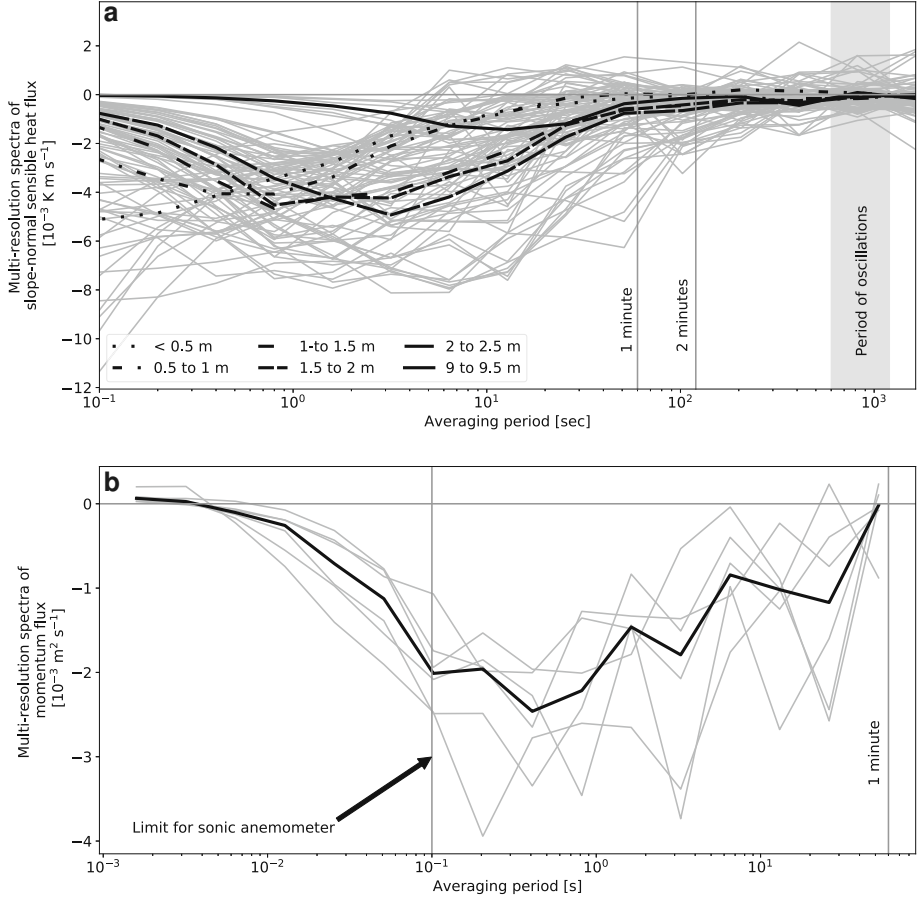


Fig. 3 **a** Multi-resolution spectra of turbulent sensible heat flux $\overline{w'\theta'}$ in the streamline-defined coordinate system for the CSAT data. Each grey line is associated with one sonic anemometer during a given katabatic event. To show the impact of height, the median is plotted by range of heights (black lines). The grey shading is the period of oscillations observed in the present dataset, associated to McNider frequency $N \sin \alpha$ (McNider 1982). **b** Multi-resolution spectra of the turbulent momentum flux $\overline{u'w'}$ for the cobra data. Each of the six 1-min datasets is represented by one grey line. The black line is the median

3.3 Cobra (Three-Dimensional Pitot-Type Sensor) Data

Cobra measurements were performed manually in the first metre of the jet along a vertical axis for 1 min at each level. The measurements were processed during the final night of the campaign (28 February 2019) at specific periods when katabatic events were reported to be well developed, and at heights with velocities above the measurement threshold of 2 m s^{-1} . Among all measurements, the purest dataset corresponds to six 1-min segments located between $z = 3 \text{ cm}$ and $z = 28 \text{ cm}$ in the period 0621–0636 (during event 7 in Table 3, Fig. 1e). A double rotation was applied to place the data in the streamline coordinate system defined in the previous section. A MRD analysis of the time series from the Cobra data suggests that 1-min averaging time was enough to measure the fluxes precisely (Fig. 3b), with a Reynolds decomposition.

4 Results and Discussion

4.1 Meteorological and Surface Energy Conditions

Ambient thermal stratification in terms of N_{ref} , estimated from the temperature profiles provided by the tethered balloon at Site B, varied between 0.012 and 0.036 Hz throughout the campaign, with a mean value of around 0.02 Hz (Fig. 2). The highest stratification values were observed in the morning and the lowest values in the late afternoon. Figure 4a shows changes in the surface temperature, air temperature, and specific humidity at about 3.5-m height over time throughout the field experiment. Surface temperature ranged from -10 to 0°C during the diurnal cycle. Note that during the day, we expect the highest surface temperature to be 0°C due to snow melt. The slightly positive values are linked to uncertainties due to the estimation of T_s from longwave radiation (Eq. 1, Fig. 4b), which is approximately 2°C . The temperature gradient close to the surface was more pronounced at night than during the day, with a difference of 15°C between the surface and the first sensor at 3.4 m height at the beginning of the experiment.

The air was relatively dry with low night-time specific humidity values ranging between 1 and 3 g kg^{-1} . For the sake of comparison, the saturated specific humidity for a temperature of 5°C is 6.5 g kg^{-1} . This requires a negligible correction of the virtual temperature versus air temperature. The three anticyclonic periods defined in Sect. 2.1 correspond to different behaviours in the specific humidity time series:

- In the very stable phase 1, humidity followed the same diurnal pattern as temperature.
- In phase 2, air humidity was higher, and the diurnal pattern was still strongly present.
- In phase 3, the behaviour of humidity was more variable and chaotic, even if high (low) Here values were still observable during the day (night).

Figure 4b shows the longwave flux at the surface. The diurnal cycle is particularly clear in the upwards longwave flux, which is directly linked to surface temperature. Its amplitude is around 30 W m^{-2} . Figure 4c shows the main term of the surface energy budget. At night, the net radiation $R_n = (LW + SW)_{\text{down}} - (LW + SW)_{\text{up}}$ (where SW stands for shortwave) is negative, as expected particularly in anticyclonic conditions. It varied between -80 and -60 W m^{-2} . The near-surface turbulent sensible heat flux, estimated by $H = \rho C_p \overline{w'\theta'}$ (with ρ the density of air and $C_p = 1004\text{ J kg}^{-1}\text{ K}^{-1}$ the specific heat for dry air at constant pressure) at the first measurement level is mostly negative at night, which reflects the cooling of the air by the surface. Values differed considerably from one night to another. We also observed variations at the scale of one night. Mean night-time values varied between -60 and -15 W m^{-2} . Figures 4d, e show wind direction with respect to the main downslope direction, and wind speed at two representative levels. Note that wind direction corresponds to the slope direction for the episodes analyzed in the present paper and this is one of the criteria we used to design such katabatic episodes.

4.2 Mean Wind Speed and Temperature Profiles

Mean streamwise velocity profiles and temperature profiles of all katabatic events presented in Sect. 2.2 are shown in Figs. 5 and 6, respectively. Sonic temperature deviation from temperature was negligible; we consequently used the sonic temperature in Fig. 6 directly (Kaimal and Finnigan 1994; Charrondière et al. 2020). Figure 5 shows that the jet peak is quite close to the surface, i.e., at a distance less than 1 m. At the end of the experiment, only the region above the height of maximum wind speed was captured.

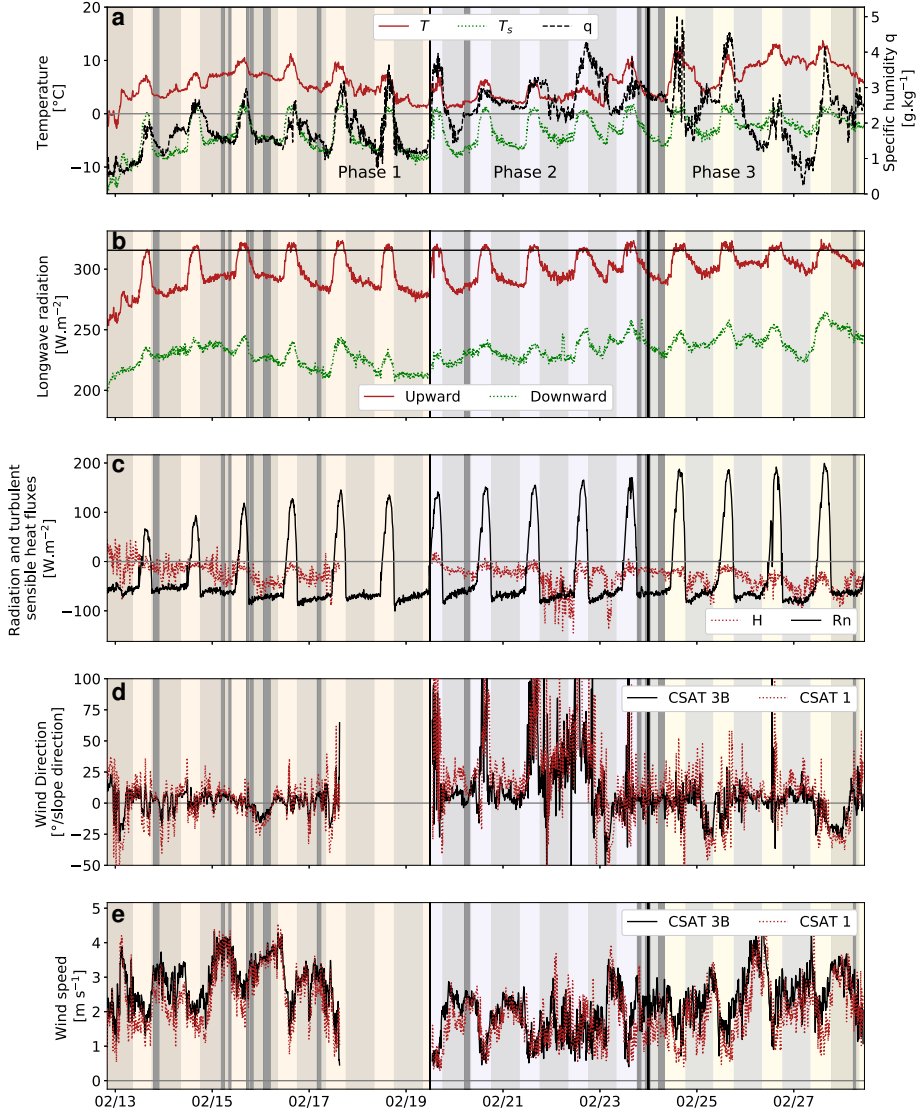


Fig. 4 **a** Changes in air temperature T , surface temperature T_s , and specific humidity q . The thermo-hygrometer that provides T and q was located 3.4 m above the surface at the beginning of the experiment. **b** Changes in longwave radiation fluxes at the surface over time. **c** Changes over time in the turbulent sensible heat flux H at the first sonic anemometer level and of the net radiation flux R_n . **d** Changes in wind direction with respect to the main downslope direction for two representatives levels (Table 1) and **e** changes in wind speed for the same two levels. Light grey regions cover nighttime, defined as the period during which shortwave radiation is below 20 W m^{-2} . Dark grey vertical shading indicates katabatic events

In this study, we fitted the wind-speed and temperature profiles with a modified version of the Prandtl model whose eddy-diffusivity coefficients varied linearly with height (Grisono and Oerlemans 2001; Brun et al. 2017; Charrondière et al. 2020). Figure 7 shows the velocity and temperature profiles measured by sonic anemometers and thermocouples, and

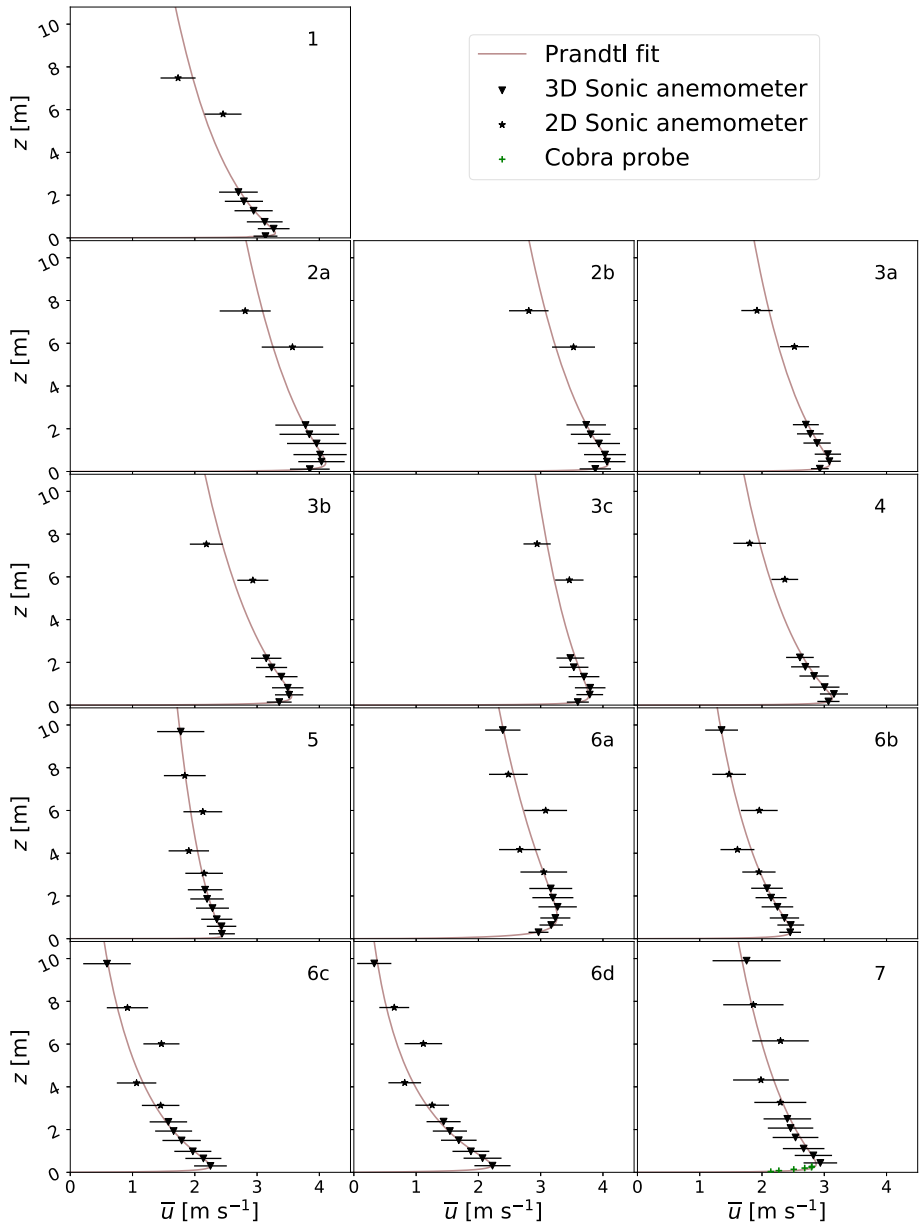


Fig. 5 Slope-normal profiles of mean streamwise velocity. The error bar is the standard deviation of the 2-min segments of each katabatic event. The green crosses in event 7 are the data from the Cobra sensor. The line is the fit derived from the Prandtl model

complemented with the data from the tethered balloon up to 50 m, from the 6d event, on 24 February between 0500 and 0800 LT. The Prandtl fit, applied only to the data from the mast, is in accordance with the tethered balloon measurements above. The wind speed decreased

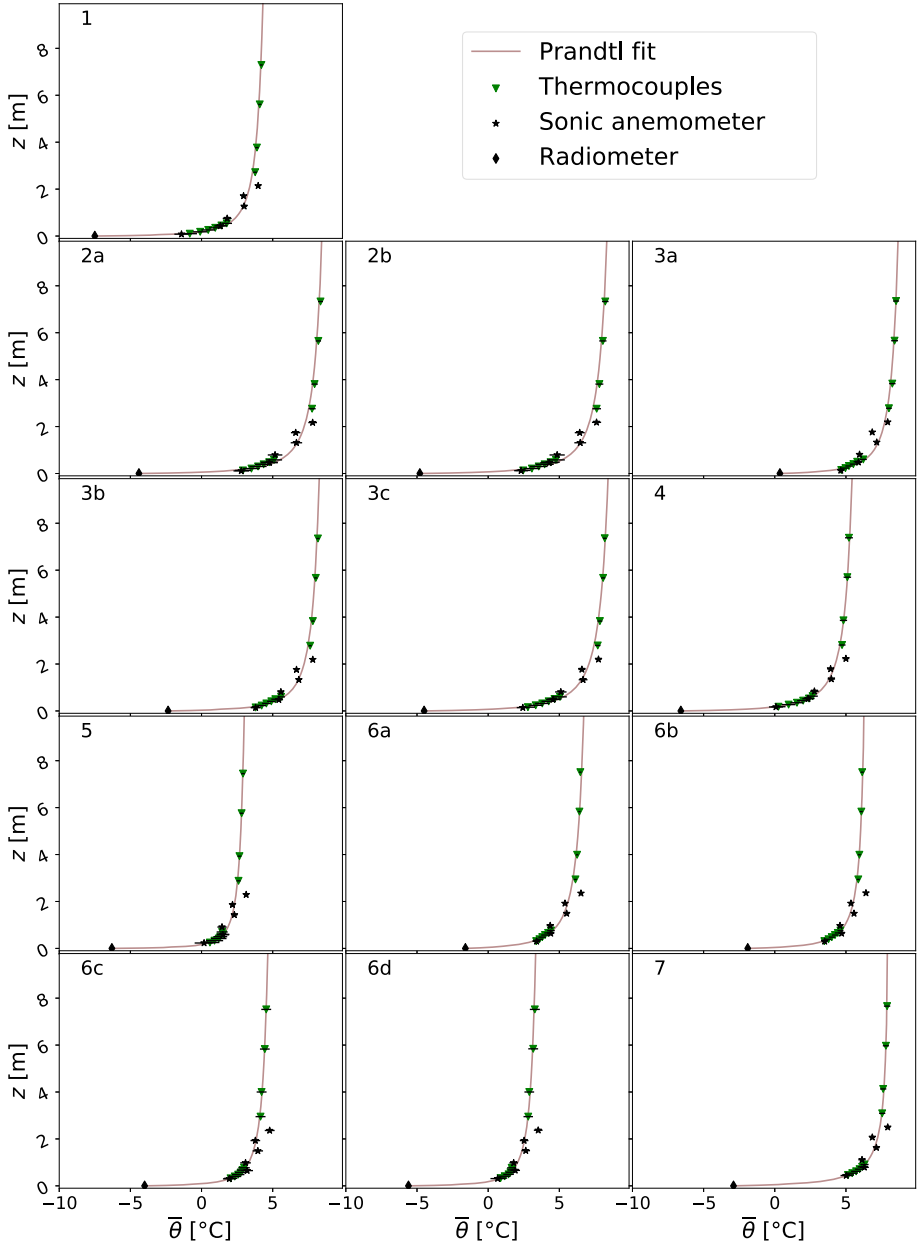


Fig. 6 Slope-normal profiles of mean temperature. The error bar is the standard deviation of the 2-min segments of each katabatic event. The line is the fit derived from the Prandtl model

to zero at a height close to 25–30 m. Above 15 m, as the katabatic wind speed decreased drastically, a low ambient wind speed of about 0.5 m s^{-1} became observable.

For this event, the Prandtl fit provides the slope normal height of the maximum wind speed at $z_j \simeq 20 - 30 \text{ cm}$ above the snow surface. Beyond all katabatic events observed during

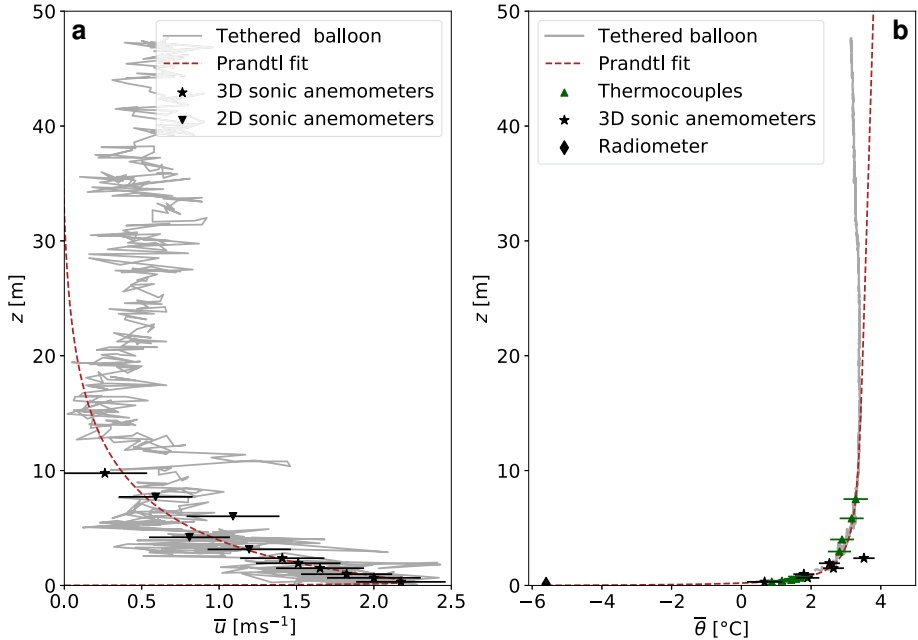


Fig. 7 **a** Streamwise wind velocity profile and **b** temperature profile during the katabatic 6d event from 0500 to 0800 LT on 24 February. The tethered balloon profile was acquired between 0700 and 0720 LT. The dots (error bars) represent the medians (standard deviations) of the 90 (2-min) segments in the katabatic event

the experiment, z_j never exceeded 1.1 m. In most cases, it was of a few tens of centimetres. In experimental studies over steep slopes, the wind-speed maximum z_j is located near the ground: around 1 m and always below 2 m with $\alpha = 21^\circ$ (Horst and Doran 1988; Charrondière et al. 2020), between 0.45 and 1.27 m with $\alpha = 35.5^\circ$ (Oldroyd et al. 2014). Low heights z_j observed in the present study may be explained by the presence of snow, which is not the case in the other steep slope studies (Table 2). Roughness was thus largely reduced: aerodynamic roughness length z_0 was of the order of 0.2 mm for fresh snow (Brock et al. 2006), compared to 20 mm in the studies of Nadeau et al. (2013b) and Oldroyd et al. (2016a), who measured katabatic winds on a rough surface with vegetation. This low surface roughness could bring the jet maximum closer to the surface (Rajaratnam 1976).

In Fig. 6, measurements by thermocouples and sonic anemometers show consistent profiles. We observed a strong temperature gradient in the first few metres above the surface. The temperature difference between the surface and 1 m ranged from 8 to 13 °C. As theoretically expected, there is a remarkably clear proportionality between the temperature gradient close to the surface and the maximum wind speed (Figs. 5, 6). Figure 7b shows that the Prandtl fit, once again determined only from the mast temperature data, follows the tethered balloon profile closely up to 15–20 m, which is approximately the thickness of the jet.

4.3 Slope-Normal Velocity in the Jet Core

Figure 8 shows the slope-normal profiles for the mean slope-normal velocity component for each katabatic event (Sect. 2.2) in the topographic coordinate system. For all the events, $\bar{w} > 0$ above $z \simeq 0.5$ m, with a maximum observed value of 0.25 m s^{-1} ($\sim 10\%$ of \bar{u}_j).

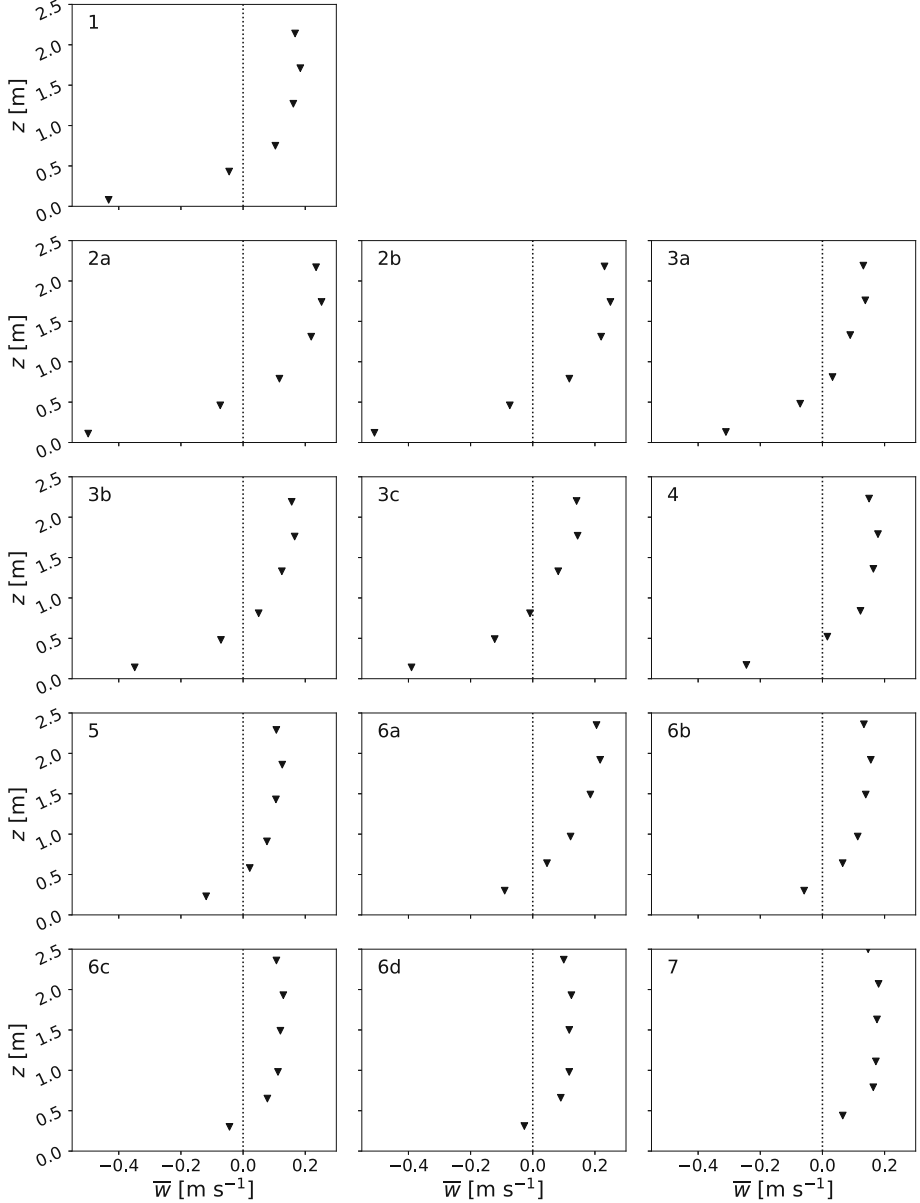


Fig. 8 Slope-normal profiles of mean slope-normal velocity component. The error bar is the standard deviation of the 2-min segments of each katabatic event. The number above the lowest measurement point is the angle (in degree) between the streamline inclination and $\alpha = 30^\circ$

Close to the surface, we measured $\bar{w} < 0$ in the fixed coordinate system which corresponds to a 30° slope (Sect. 3.2) determined using a 25-m resolution DEM (Sect. 2.1). These negative slope-normal velocity values would suggest that the local slope is steeper: $\alpha \simeq 38^\circ$ is the slope angle necessary to nullify \bar{w} at the first measurement level for the first katabatic event. Nevertheless, we decided to keep the average slope angle of 30° to define the fixed coordinate

system since it is more consistent with the whole \bar{w} profile behaviour. Whatever the chosen angle, we observe a significant variation of \bar{w} from the surface up to $z \simeq 2.5$ m. This variation is of the order of 0.75 m s^{-1} , which corresponds to 25% of \bar{u}_j .

Furthermore, streamline inclination in the first tens of centimetres of the jet could be influenced by local effects such as micro-topography and modification of the snow surface downstream the measurement mast during the set-up of the experiment. Only the lowest measurement points are likely to be affected in this case. The resulting streamline angle deviation is given for quantification on Fig. 8 at the first measurement level.

In most of the events, there was also a slight decrease of \bar{w} at the (two) upper measurement levels. This is consistent with the behaviour observed by Eriksson et al. (1998) for a wall jet, where \bar{w} became negative in the upper part of the jet, above a positive \bar{w} region.

To our knowledge, measurements of slope-normal velocity component inside the jet have never been made in experimental studies of katabatic flows. This result calls into question the assumption that streamlines are parallel to the topography close to the surface, which is usually the starting statement when processing sonic anemometer data and defining the working coordinate system. The present results show that the streamline-defined coordinate systems (Sect. 3.2) are quite different from one level to another.

4.4 Turbulent Momentum Flux in the Inner Layer

Figure 9 shows the main turbulent momentum flux profile $\overline{u'w'}(z)$ determined from sonic anemometers for the 16 min of event 7 for which the Cobra probe was used (Table 3, Sect. 3.3), and from the Cobra data. The sonic anemometers, data are presented in the two coordinate systems defined in Sect. 3.2, i.e., the streamline coordinate system $(\vec{x}_s, \vec{y}_s, \vec{z}_s)$ and the topographic coordinate system $(\vec{x}, \vec{y}, \vec{z})$. Maximum wind speed is located in the grey shaded region, at $z_j \simeq 40$ cm following the Prandtl fit (Fig. 5, event 7). The turbulent momentum flux was positive in the upper part of the jet and negative in the lower part, as expected from the Boussinesq hypothesis (Boussinesq 1877). The difference between values in the two coordinate systems is due to redistribution of part of the variances $\overline{u'^2}$ and $\overline{w'^2}$ into $\overline{u'w'}$. While the choice of the coordinate system does not affect the main behaviour of the turbulent momentum flux, the height at which $\overline{u'w'}$ cancels is sensitive to it. For the 30° topographic coordinate system, it is closer to the maximum-wind-speed region even if there is still a shift between the maximum-wind-speed height and the height at which $\overline{u'w'}$ cancels (Charrondière et al. 2020). The choice of the coordinate system also affects the magnitude of the momentum flux.

In the inner part of the katabatic jet, the magnitude of the turbulent momentum flux increases near the surface. Despite the low measurement heights, we observed no constant flux layer. This is consistent with the analytical profile defined based on the scale analysis of the equation of momentum by Denby and Smeets (2000). In the first approximation, katabatic forcing balances the turbulent momentum flux gradient in the inner part of the jet, which results in Eq. 3

$$\overline{u'w'}(z) = \frac{g \sin \alpha}{\theta_{ref}} \int_z^{Z_1} (\bar{\theta} - \theta_{ref}) \partial z + \overline{u'w'}(Z_1). \quad (3)$$

Here θ_{ref} is the ambient potential temperature profile, and Z_1 is taken close to the maximum wind-speed height, at the first sonic measurement level ($z = 44$ cm). Equation 3 was applied in Fig. 9, in the fixed 30° coordinate system (black dashed line). The behaviour of the modelled turbulent momentum flux is consistent with the data. The main difference may be due to the

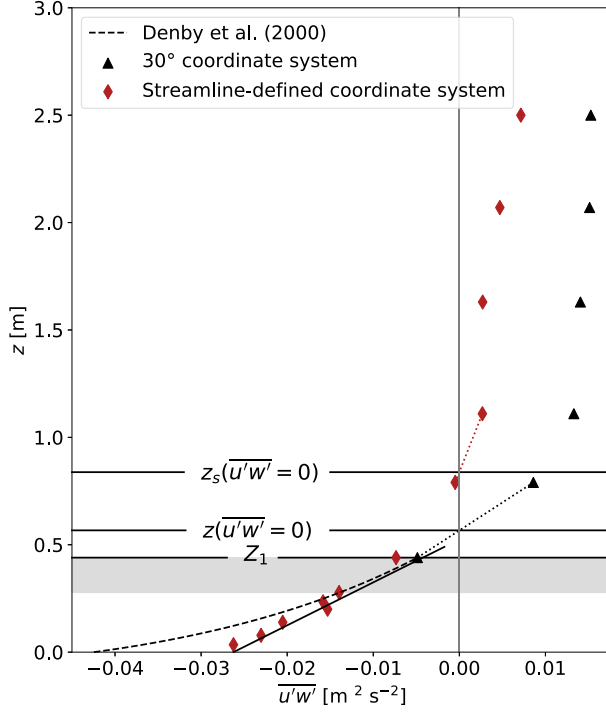


Fig. 9 Main turbulent momentum flux during the katabatic event on 28 February between 0530 and 0636 LT. Triangles and diamonds represent sonic anemometers data. Stars represent data from the Cobra probe. The coordinate systems are named with reference to Sect. 3.1. The black dashed line is the analytical profile defined in Denby and Smeets (2000). Dotted lines are linear interpolation to estimate the height at which $\overline{u'w'} = 0$. The black solid line is the linear approximation $\overline{u'w'} = -u_*^2(1 - az)$, with $a = 1.9 \text{ m}^{-1}$. The grey shading is the region in which the maximum wind speed is located

streamline coordinate system in which the Cobra data are presented, since we did not have access to the topographic coordinate system.

4.5 Time-Resolved Data Using the Cobra Probe

Thanks to the small measuring volume associated with the size of the Cobra probe (its head is 2.6 mm wide), it was possible to perform acquisition very close to the surface (down to $z = 3 \text{ cm}$, Sect. 2) and with a high temporal frequency (1250 Hz). This is a big advantage to accurately describe the turbulent boundary layer very close to the surface compared to what is generally done with sonic anemometry.

4.5.1 Investigation of the Wind-Velocity Profile Close to the Surface

Figure 10a shows the profile of the streamwise velocity \bar{u} , with the six levels acquired with the Cobra probe and all the sonic anemometers during event 7 (Table 3). Reynolds number Re defined based on the maximum wind speed u_j and height z_j ($Re = z_j u_j / \nu$) is of the order 10^4 – 10^5 for the studied katabatic winds. With such high Re values, the viscous sub-layer is very thin and the first measurement level at $z = 3 \text{ cm}$ height, well beyond it, is already

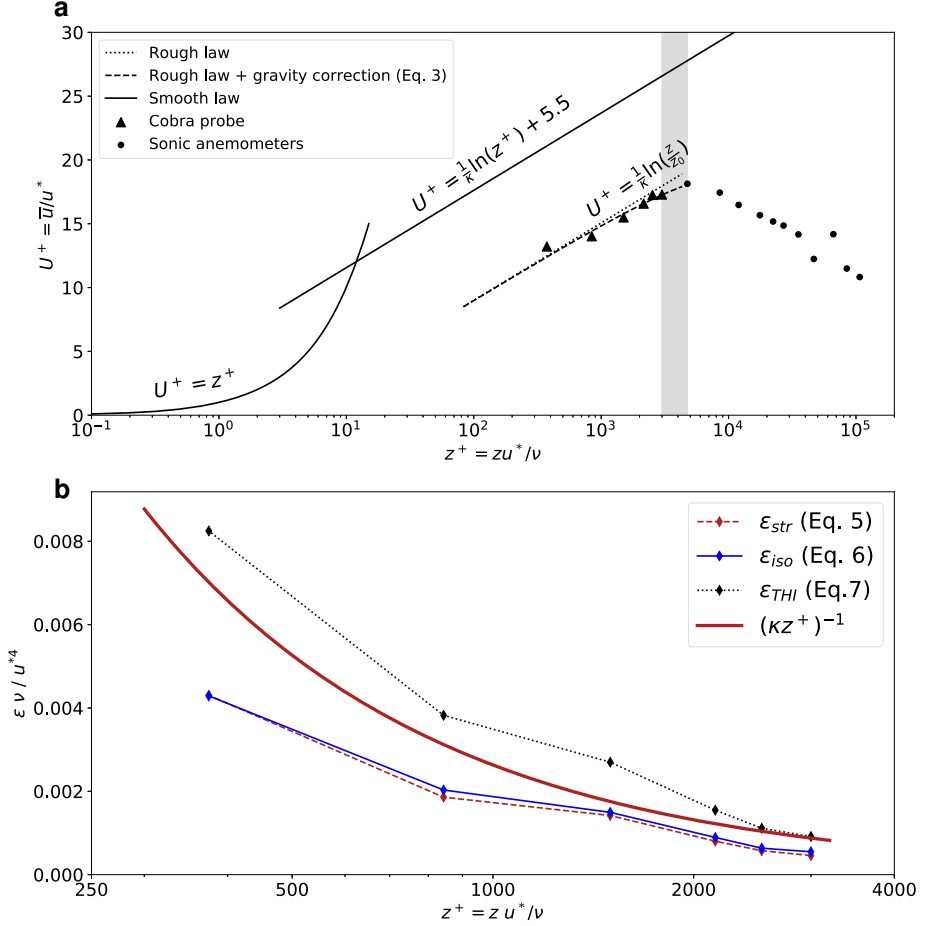


Fig. 10 **a** Normalized streamwise wind velocity profile acquired during the event 7. The grey shading is the region in which the maximum wind speed is located. $z_0 = 0.3$ mm and $\kappa = 0.38$. **b** Normalized dissipation rate of TKE for the inner layer of the jet, including the theoretical decaying law for a turbulent boundary layer above a flat surface $\varepsilon = u_*^3/(\kappa z)$

in the fully turbulent layer. The wind speed \bar{u} is thus normalized with the friction velocity $u_* = \sqrt{|u'w'|}$ taken at this level, located at $z^+ = zu_*/\nu = 375$ height, with ν the kinematic viscosity of air ($\nu = 15.10^{-6} \text{ m}^2 \text{ s}^{-1}$). On a rough surface, the velocity profile follows a law of the form $U^+ = \bar{u}/u_* = (1/\kappa) \ln z/z_0$ (Schultz and Flack 2007), with $\kappa = 0.38$ for the von Kármán constant (Andreas et al. 2006; Foken 2006; Segalini et al. 2013) and z_0 the aerodynamic roughness length. In katabatic flows, the momentum flux $\overline{u'w'}$ is not constant over height z (Denby and Smeets 2000). According to the present observations, it can be approximated by $-\overline{u'w'} = u_*^2(1 - az)$, with $a = 1.9 \text{ m}^{-1}$. This correction term is added in the classical velocity profile logarithmic law, which results in a new law including a logarithmic term and a linear term:

$$\bar{u}/u_* = \frac{1}{\kappa} \ln \frac{z}{z_0} - \frac{a}{2\kappa} z. \quad (4)$$

In boundary layers over flat surfaces, this law also includes a correction due to the buoyancy effect proportional to z/L_{MO} , where L_{MO} is the Obukhov length (Zilitinkevich and Calanca 2000). In the present case, this latter correction is negligible, with $z/L_{MO} \sim 0.002$ at the first sonic anemometer level ($z = 44$ cm). The classical logarithmic law (for $\overline{u'w'}$ constant) seems to be in good accordance with the experimental data below the maximum-wind-speed height z_j . This means that, as expected, the inner layer of the katabatic jet behaves like a classical turbulent boundary layer. The correction term due to $\overline{u'w'}$ variation with z has been added to Fig. 3. The law including this term (Eq. 4) better fits the data, but the correction is very small, reaching only $\sim 0.1 \text{ m s}^{-1}$ at the highest measurement level ($z = 28$ cm), which is only 4% of maximum velocity.

While the presence of a logarithmic law has been observed in the inner part of plane wall jets (Myers et al. 1961; Tachie et al. 2002; Villafruela et al. 2008), and even in gravity currents (Kneller et al. 1999, for example), it has never been experimentally shown to hold in katabatic flows, particularly over a steep slope. Furthermore, in our case, this law holds in the range z^+ of [375, 3000], which is a high value compared to those achieved laboratory turbulent boundary layers. As a comparison, the logarithmic region was observed only up to $z^+ \simeq 70$ in Kneller et al. (1999) and only reached a few hundred in Tachie et al. (2002) and Villafruela et al. (2008).

The roughness length z_0 was experimentally determined with the logarithmic velocity profile assumption, and was about 0.3 mm. This result is in accordance with the 0.2 mm provided by Brock et al. (2006) for fresh snow (Sect. 4.2). The last snowfall occurred 2–3 weeks before the katabatic event, and roughness would thus be expected to be a little higher than above very fresh snow because of melting, compacting, and erosion of snow.

4.5.2 Spectral Analysis of Turbulence Close to the Surface

Figure 10b shows the normalized dissipation term from the TKE budget. Its value was determined from the second order structure function of \bar{u} (Morales et al. 2012), by assuming Kolmogorov scaling (Eq. 5). We also determined its value from the analytical formula (Pope 2000) after applying the Taylor hypothesis and isotropy assumption (Eq. 6) and after also applying the homogeneity assumption (Eq. 7),

$$\varepsilon_{str} = \frac{1}{r} \left(\frac{\langle \delta u(r)^2 \rangle}{C_2} \right)^{3/2} \quad \text{with } C_2 = 2, \quad (5)$$

$$\varepsilon_{iso} = \frac{3\nu}{\bar{u}^2} \left[\overline{\left(\frac{\partial u'}{\partial t} \right)^2} + \overline{\left(\frac{\partial v'}{\partial t} \right)^2} + \overline{\left(\frac{\partial w'}{\partial t} \right)^2} \right], \quad (6)$$

$$\varepsilon_{THI} = \frac{15\nu}{\bar{u}^2} \overline{\left(\frac{\partial u'}{\partial t} \right)^2}. \quad (7)$$

The dissipation rate increases close to the surface, consistently with what is obtained in turbulent boundary layers (TBL, Pope 2000). The dissipation law $\varepsilon = 1/\kappa z^+$ valid in the logarithmic layer for a TBL over a flat surface slightly overestimates ε when $\kappa = 0.38$ is set. This could be related to the fact that the dissipation length would increase due to gravity effects over a steep slope. Further work is necessary to clarify this issue. The difference between the two curves ε_{iso} and ε_{THI} shows that the homogeneity assumption is far from

valid. The dissipation rates determined from the second order structure function ε_{str} and in the isotropic case ε_{iso} are remarkably close. This means that the acquisition frequency of the Cobra sensor ($f = 1250$ Hz) is high enough to accurately evaluate the dissipation rate, which is an approach rarely used previously. In the following, we thus use ε_{iso} .

Figure 11 shows the normalized streamwise and slope-normal velocity spectra for the 1-min series acquired with the Cobra sensor at $z = 23$ cm and $z = 3$ cm (Sect. 3.3). The transformation from the temporal domain to the spatial domain is achieved with the method used in Buchhave and Velte (2017), which derives from the Taylor hypothesis. Here we provide an evaluation of the spectral characteristic length scales (Pope 2000):

- The integral length scale, $L = \int_0^{r_0} R_{uu} dr \simeq 1.13$ m, is calculated with the streamwise velocity autocorrelation function R_{uu} , with r determined thanks to the Taylor hypothesis. r_0 is the lowest value of r for which $R_{uu} = 0$. The integral length scale represents the size of the larger scales of turbulence, which contain most of the turbulence kinetic energy.
- The Taylor scale, $\lambda = \sqrt{15\nu u'^2 / \varepsilon_{iso}} \simeq 2.4$ cm, is the scale from which viscosity effects become not negligible with respect to other mechanisms.
- The Kolmogorov microscale, $\eta = \nu^{3/4} / \varepsilon_{iso}^{1/4} \simeq 0.6$ mm, represents the smallest turbulence scale of the flow.

An inertial subrange for the velocity spectra following a $-5/3$ slope is well developed and covers nearly two decades up to the Taylor scale λ for the two measurement levels acquired with the Cobra sensor. This is consistent with high Taylor Reynolds number $Re_\lambda = u'\lambda/\nu$ of 400 at the lowest measurement level ($z = 3$ cm height). At higher wavenumbers, between λ and η , dissipation is the dominant process leading to an experimental decrease of the spectra. The Kolmogorov microscale is not captured in the spectra, but its value is of an order of magnitude that allows good estimation of the dissipation rate using the analytical formula. The 1-min time series are also long enough to integrate precisely the integral scale L .

To enable a comparison, Fig. 11 also shows streamwise and slope-normal velocity spectra from the lower sonic anemometer at $z = 0.44$ m, throughout the associated event 7 (28 February between 0530 and 0636, Table 3). The sampling frequency, which is two orders of magnitude lower than that of the Cobra sensor, does not enable the dissipation rate to be estimated directly from the structure function. Instead, we used the inertial subrange formula $S_u(k_x) = \alpha_\kappa \varepsilon^{2/3} k_x^{-5/3}$ to evaluate ε with $\alpha_\kappa = 0.5$ (Stull 1988), which is equivalent to the structure function method in terms of hypothesis. As expected, given the greater height of the sonic anemometer with respect to the Cobra probe, the characteristic scales shifted to higher values: $L \simeq 65$ m, $\lambda \simeq 8.7$ cm and $\eta \simeq 0.86$ mm. We observed the inertial subrange for only one decade, including most of the energy containing scales of the flow.

Investigating turbulence in the first tenths of centimetres above the surface with sonic anemometry is known to be difficult: the sampling volume and frequency are not really suitable for the small scales expected close to the surface and measurement accuracy may be a problem. The present Cobra data validate the data from the sonic anemometers and are evidence that the quality of sonic measurements may be sufficient to capture most of the scales, at least down to 44 cm in the present katabatic conditions.

The sonic anemometer spectra were determined with a series of more than 1 min (96 min in this case), which made it possible to observe a plateau-like trend at low wavenumbers on the slope-normal velocity spectra.

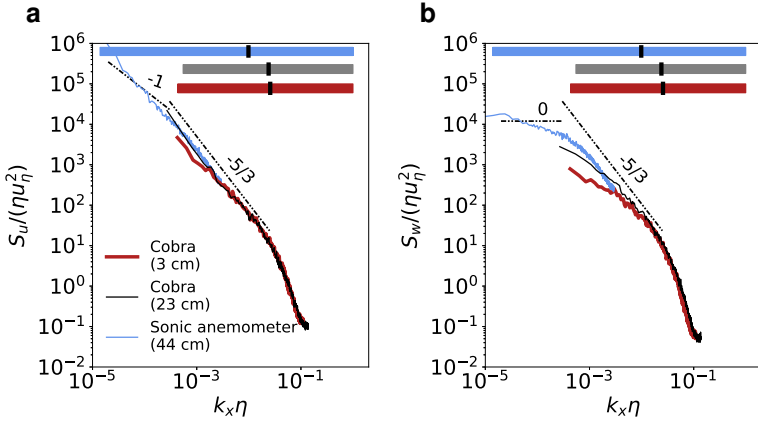


Fig. 11 **a** Spectra of the 1-min streamwise wind velocity series at $z = 3$ cm (red) and $z = 23$ cm (grey) for the Cobra probe and from the lower sonic anemometer (blue) at $z = 44$ cm during the katabatic event on 28 February between 0530 and 0636 LT. For the sonic anemometer, the streamwise velocity was taken from the fixed coordinate system defined in Sect. 3. The spectra is normalized with the Kolmogorov length and velocity scales. **b** Same figure for the slope-normal velocity spectra. Horizontal thick lines delineate the range of wavenumbers between the integral scale L on their left side and the Kolmogorov scale η on their right side. The colour of the line is associated with the curve of the same color. The black symbol on these lines is Taylor scale λ .

5 Conclusion

This paper presents an in-situ experiment conducted over a steep snow-covered slope to study katabatic flow. It was designed to solve some outstanding issues, particularly lacking in the experimental field. We first presented an overview of the full potential of this new dataset. It is rich both in terms of mean quantities for the linkage between the katabatic jet and its environment due to the use of a tethered balloon, and in terms of turbulence properties, particularly in the inner region.

Preliminary results show profiles of slope-normal velocity, which is far from being negligible and reached 0.25 m s^{-1} above the maximum wind speed height in the present experiment, which corresponds to about 10% of the maximum streamwise velocity of the jet. This raises some questions about the choice of the coordinate system used to represent the results, which directly affects the magnitude of turbulent fluxes, as shown here for the turbulent momentum flux $\overline{u'w'}$. The height at which this flux changes sign is also sensitive to the coordinate system used, with consequences for the redistribution of the mechanical shear production terms for the turbulence kinetic energy budget.

The use of a three-dimensional pitot probe makes it possible to take measurements close to the ground (i.e. down to a distance of 3 cm) with a high sampling frequency of 1250 Hz. To our knowledge, this is completely new for in-situ experiments and provides insights into the inner part of such katabatic flows. We observed a well-developed logarithmic law with a slight correction due to gravity effects on $\overline{u'w'}$, up to a height of about $z^+ = 3000$ in terms of wall units. This makes the inner part of the present flow comparable to a turbulent boundary layer.

Turbulence data from the three-dimensional pitot probe are also insightful: the inertial subrange of the velocity spectra is well resolved. The spectrum also provides part of the dissipation zone at high frequency and covers the integral length scale at low frequency.

These data offer the opportunity to study turbulence in the inner region of katabatic jets, and in more generally, in the lower part of the turbulent boundary layer in the case of in-situ measurements. The turbulence data also confirm the quality of the results obtained with sonic anemometers for heights as low as 44 cm, which in the literature is often considered too low to capture turbulence correctly.

Acknowledgements This work was supported by the French National program LEFE (Les Enveloppes Fluides et l'Environnement) under the application COCA AO INSU LEFE 2021 and by a Grant from Labex OSUG@2020 (Investissements d'avenir ANR10 LABX56). We would like to thank J. Dagaut, M. Guilbot, A. Martin, H. Michallet, M. Obligado, C. Poncet, I. Redor, L. Seguinot and T. Sue for their participation to the field experiment. We also would like to thank the city administration of Revel (38420, France) for their logistical support.

References

- Andreas EL, Claffey KJ, Jordan RE, Fairall CW, Guest PS, Persson POG, Grachev AA (2006) Evaluations of the Von Kármán constant in the atmospheric surface layer. *J Fluid Mech* 559:117
- Baldocchi DD (2003) Assessing the eddy covariance technique for evaluating carbon dioxide exchange rates of ecosystems: past, present and future. *Glob Change Biol* 9(4):479–492
- Blein S (2016) Observation and modelisation of stable atmospheric boundary layer in complex topography: turbulent processes of katabatic flows (in French). Ph.D. thesis, Université Grenoble Alpes, France
- Boussinesq J (1877) Essai sur la théorie des eaux courantes. *C R Acad Sci* 87:1–680
- Brock BW, Willis IC, Sharp MJ (2006) Measurement and parameterization of aerodynamic roughness length variations at Haut Glacier d'Arolla, Switzerland. *J Glaciol* 52(177):281–297
- Brun C, Blein S, Chollet J (2017) Large-eddy simulation of a katabatic jet along a convexly curved slope. Part 1: statistical results. *J Atmos Sci* 74(12):4047–4073
- Buchhave P, Velte CM (2017) Measurement of turbulent spatial structure and kinetic energy spectrum by exact temporal-to-spatial mapping. *Phys Fluids* 29(8):085,109
- Charrondière C, Brun C, Jean-Emmanuel S, Cohard JM, Biron R, Blein S (2020) Buoyancy effects in the turbulence kinetic energy budget and Reynolds stress budget for a katabatic jet over a steep alpine slope. *Boundary-Layer Meteorol* 177(1):97–122
- Davies J, Robinson P, Nunez M (1971) Field determinations of surface emissivity and temperature for Lake Ontario. *J Appl Meteorol* 10(4):811–819
- Denby B, Smeets C (2000) Derivation of turbulent flux profiles and roughness lengths from katabatic flow dynamics. *J Appl Meteorol* 39(9):1601–1612
- Dozier J, Warren SG (1982) Effect of viewing angle on the infrared brightness temperature of snow. *Water Resour Res* 18(5):1424–1434
- Duynkerke PG, Van den Broeke MR (1994) Surface energy balance and katabatic flow over glacier and tundra during GIMEX-91. *Glob Planet Change* 9(1–2):17–28
- Eriksson J, Karlsson R, Persson J (1998) An experimental study of a two-dimensional plane turbulent wall jet. *Exp Fluids* 25(1):50–60
- Fedorovich E, Shapiro A (2009) Structure of numerically simulated katabatic and anabatic flows along steep slopes. *Acta Geophys* 57(4):981–1010
- Finnigan J, Ayotte K, Harman I, Katul G, Oldroyd H, Patton E, Poggi D, Ross A, Taylor P (2020) Boundary-layer flow over complex topography. *Boundary-Layer Meteorol* 177:247–313
- Foken T (2006) 50 Years of the Monin–Obukhov similarity theory. *Boundary-Layer Meteorol* 119(3):431–447
- Geiger R, Aron RH, Todhunter P (2009) *The climate near the ground*. Rowman & Littlefield, Lanham
- Grachev AA, Leo LS, Di Sabatino S, Fernando HJS, Pardyjak ER, Fairall CW (2016) Structure of turbulence in katabatic flows below and above the wind-speed maximum. *Boundary-Layer Meteorol* 159(3):469–494
- Grisogono B, Oerlemans J (2001) Katabatic flow: analytic solution for gradually varying eddy diffusivities. *J Atmos Sci* 58(21):3349–3354
- Haiden T, Whiteman CD (2005) Katabatic flow mechanisms on a low-angle slope. *J Appl Meteorol* 44(1):113–126
- Helmis C, Papadopoulos K (1996) Some aspects of the variation with time of katabatic flow over a simple slope. *Q J R Meteorol Soc* 122(531):595–610
- Horst T, Doran J (1988) The turbulence structure of nocturnal slope flow. *J Atmos Sci* 45(4):605–616

- Horst T, Semmer S, Maclean G (2015) Correction of a non-orthogonal, three-component sonic anemometer for flow distortion by transducer shadowing. *Boundary-Layer Meteorol* 155(3):371–395
- Howell J, Mahrt L (1997) Multiresolution flux decomposition. *Boundary-Layer Meteorol* 83(1):117–137
- Jensen DD, Nadeau DF, Hoch SW, Pardyjak ER (2017) The evolution and sensitivity of katabatic flow dynamics to external influences through the evening transition. *Q J R Meteorol Soc* 143(702):423–438
- Kaimal JC, Finnigan JJ (1994) *Atmospheric boundary layer flows: their structure and measurement*. Oxford University Press, New York
- Kneller BC, Bennett SJ, McCaffrey WD (1999) Velocity structure, turbulence and fluid stresses in experimental gravity currents. *J Geophys Res Oceans* 104(C3):5381–5391
- Krug D, Holzner M, Lüthi B, Wolf M, Kinzelbach W, Tsinober A (2013) Experimental study of entrainment and interface dynamics in a gravity current. *Exp Fluids* 54(5):1530
- Largeroy Y, Staquet C (2016) Persistent inversion dynamics and wintertime PM₁₀ air pollution in alpine valleys. *Atmos Environ* 135:92–108
- Litt M, Sicart JE, Helgason WD, Wagnon P (2015) Turbulence characteristics in the atmospheric surface layer for different wind regimes over the Tropical Zongo Glacier (Bolivia, 16° S). *Boundary-Layer Meteorol* 154(3):471–495
- Litt M, Sicart JE, Six D, Wagnon P, Helgason WD (2017) Surface-layer turbulence, energy balance and links to atmospheric circulations over a mountain glacier in the French Alps. *Cryosphere* 11(2):971–987
- Low PS (1990) Katabatic winds in the lower Tamar Valley, Tasmania. *Il Nuovo Cimento C* 13(6):981–994
- Manins P, Sawford B (1979) A model of katabatic winds. *J Atmos Sci* 36(4):619–630
- McNider RT (1982) A note on velocity fluctuations in drainage flows. *J Atmos Sci* 39(7):1658–1660
- Monti P, Fernando H, Princevac M, Chan W, Kowalewski T, Pardyjak E (2002) Observations of flow and turbulence in the nocturnal boundary layer over a slope. *J Atmos Sci* 59(17):2513–2534
- Morales A, Wächter M, Peinke J (2012) Characterization of wind turbulence by higher-order statistics. *Wind Energy* 15(3):391–406
- Myers G, Schauer J, Eustis R (1961) The plane turbulent wall jet. Part 1: jet development and friction factor. Technical report, Department of Mechanical Engineering, Stanford University
- Nadeau D, Pardyjak E, Higgins C, Huwald H, Parlange M (2013a) Flow during the evening transition over steep alpine slopes. *Q J R Meteorol Soc* 139(672):607–624
- Nadeau D, Pardyjak E, Higgins C, Parlange M (2013b) Similarity scaling over a steep alpine slope. *Boundary-Layer Meteorol* 147(3):401–419
- Oldroyd HJ, Katul G, Pardyjak ER, Parlange MB (2014) Momentum balance of katabatic flow on steep slopes covered with short vegetation. *Geophys Res Lett* 41(13):4761–4768
- Oldroyd H, Pardyjak E, Higgins C, Parlange M (2016a) Buoyant turbulent kinetic energy production in steep-slope katabatic flow. *Boundary-Layer Meteorol* 161(3):405–416
- Oldroyd H, Pardyjak E, Huwald H, Parlange M (2016b) Adapting tilt corrections and the governing flow equations for steep, fully three-dimensional, mountainous terrain. *Boundary-Layer Meteorol* 159(3):539–565
- Pope SB (2000) *Turbulent flows*. Cambridge University Press, Cambridge
- Poulos G, Zhong S (2008) An observational history of small-scale katabatic winds in mid-latitudes. *Geogr Compass* 2(6):1798–1821
- Prandtl L (1942) *Führer durch die strömungslehre*. F Vieweg & Sohn, Braunschweig
- Princevac M, Fernando H, Whiteman CD (2005) Turbulent entrainment into natural gravity-driven flows. *J Fluid Mech* 533:259–268
- Princevac M, Hunt J, Fernando H (2008) Quasi-steady katabatic winds on slopes in wide valleys: hydraulic theory and observations. *J Atmos Sci* 65(2):627–643
- Rajaratnam N (1976) *Turbulent jets*. Elsevier, Amsterdam
- Rotach MW, Stiperski I, Fuhrer O, Goger B, Gohm A, Obleitner F, Rau G, Sfyri E, Vergeiner J (2017) Investigating exchange processes over complex topography: the Innsbruck Box (i-Box). *Bull Am Meteorol Soc* 98(4):787–805
- Schultz M, Flack K (2007) The rough-wall turbulent boundary layer from the hydraulically smooth to the fully rough regime. *J Fluid Mech* 580:381
- Segalini A, Örlü R, Alfredsson PH (2013) Uncertainty analysis of the Von Kármán constant. *Exp Fluids* 54(2):1460
- Shapiro A, Fedorovich E (2014) A boundary-layer scaling for turbulent katabatic flow. *Boundary-Layer Meteorol* 153(1):1–17
- Smeets C, Duynderke P, Vugts H (1998) Turbulence characteristics of the stable boundary layer over a mid-latitude glacier. Part 1: a combination of katabatic and large-scale forcing. *Boundary-Layer Meteorol* 87(1):117–145

- Steeneveld, GJ and Wokke, MJJ and Groot Zwaaftink, CD and Pijlman, S and Heusinkveld, BG and Jacobs, AFG and Holtslag, AAM (2010) Observations of the radiation divergence in the surface layer and its implication for its parameterization in numerical weather prediction models. *J Geophys Res Atmos* 115(D6):1–13. Wiley Online Library
- Stiperski I, Holtslag AA, Lehner M, Hoch SW, Whiteman CD (2020) On the turbulence structure of deep katabatic flows on a gentle mesoscale slope. *Q J R Meteorol Soc* 146:1206–1231
- Stull R (1988) An introduction to boundary layer meteorology, vol 126. Kluwer Academic Publishers, Dordrecht
- Sun J (2007) Tilt corrections over complex terrain and their implication for CO₂ transport. *Boundary-Layer Meteorol* 124(2):143–159
- Sun J, Oncley SP, Burns SP, Stephens BB, Lenschow DH, Campos T, Monson RK, Schimel DS, Sacks WJ, De Wekker SF et al (2010) A multiscale and multidisciplinary investigation of ecosystem–atmosphere CO₂ exchange over the rocky mountains of Colorado. *Bull Am Meteorol Soc* 91(2):209–230
- Tachie M, Balachandar R, Bergstrom D (2002) Scaling the inner region of turbulent plane wall jets. *Exp Fluids* 33(2):351–354
- Van Den Broeke MR (1997) Momentum, heat, and moisture budgets of the katabatic wind layer over a midlatitude glacier in summer. *J Appl Meteorol* 36(6):763–774
- Van Den Broeke MR, Duynkerke PG, Henneken EA (1994) Heat, momentum and moisture budgets of the katabatic layer over the melting zone of the west Greenland ice sheet in summer. *Boundary-Layer Meteorol* 71(4):393–413
- Vickers D, Mahrt L (2003) The cospectral gap and turbulent flux calculations. *J Atmos Ocean Technol* 20(5):660–672
- Villafruela J, Castro F, Parra M (2008) Experimental study of parallel and inclined turbulent wall jets. *Exp Therm Fluid Sci* 33(1):132–139
- Whiteman CD (2000) Mountain meteorology: fundamentals and applications. Oxford University Press, New York
- Wilczak J, Oncley S, Stage S (2001) Sonic anemometer tilt correction algorithms. *Boundary-Layer Meteorol* 99(1):127–150
- Zilitinkevich S, Calanca P (2000) An extended similarity theory for the stably stratified atmospheric surface layer. *Q J R Meteorol Soc* 126(566):1913–1923